

# Control of semiconductor emitter frequency by increasing polariton momenta

Yaniv Kurman<sup>1\*</sup>, Nicholas Rivera<sup>2</sup>, Thomas Christensen<sup>2</sup>, Shai Tseses<sup>1</sup>, Meir Orenstein<sup>1</sup>, Marin Soljačić<sup>2</sup>, John D. Joannopoulos<sup>2</sup> and Ido Kaminer<sup>1\*</sup>

**Light emission and absorption is fundamentally a joint property of both an emitter and its optical environment. Nevertheless, because of the much smaller momenta of photons compared with electrons at similar energies, the optical environment typically modifies only the emission/absorption rates, leaving the emitter transition frequencies practically an intrinsic property. We show here that surface polaritons, exemplified by graphene plasmons, but also valid for other types of polariton, enable substantial and tunable control of the transition frequencies of a nearby quantum well, demonstrating a sharp break with the emitter-centric view. Central to this result is the large momenta of surface polaritons that can approach the momenta of electrons and impart a pronounced non-local behaviour to the quantum well. This work facilitates non-vertical optical transitions in solids and empowers ongoing efforts to access such transitions in indirect-bandgap materials, such as silicon, as well as enriching the study of non-locality in photonics.**

Our understanding of light–matter interactions has been instrumental to a range of scientific and technological breakthroughs. At the heart of the theory of light–matter interactions lies the quantized nature of electronic transitions in matter (for example, atoms, molecules, solids, and quantum dots and wells). Indeed, this notion of quantization is critical to the understanding of both light emission and absorption, enabling key photonic technologies ranging from lasers<sup>1</sup> and light-emitting diodes (LEDs)<sup>2</sup> to charge-coupled device (CCD) photodetectors<sup>3</sup> and solar cells<sup>4</sup>.

By modifying the local optical environment of an emitter, the relative amplitude of the various transitions can be controlled with great fidelity through the Purcell effect<sup>5–7</sup>. The Purcell effect modifies the emission/absorption spectrum by enhancing the transition rate at certain frequencies and inhibiting others (that is, it alters the local density of photonic states)<sup>8,9</sup>. The transition frequencies themselves, however, are generally perturbed only very weakly by the electromagnetic environment through effects like the Lamb shift when staying in weak coupling regimes<sup>10–15</sup>, becoming, in effect, a fixed property of the emitter. Even in solids, where the electronic band structure contains a continuous range of electron energies, the absorption and emission frequencies are generally considered fixed by the electronic bandgap and the quasi Fermi levels. The transition frequencies are fixed because of the small momentum of the photons relative to that of the electrons, which effectively excludes all purely optical non-vertical/indirect transitions, although indirect processes such as phonon-mediated transitions can occur but are relatively inefficient<sup>4</sup>. The impact of the small photon momentum reappears in diverse guises throughout the study of light–matter interaction<sup>16</sup>. A pertinent question, then, is whether this large momentum difference can be bridged efficiently by directly increasing the momentum of the optical component without requiring an intermediate process.

Here we show that polaritons in thin films or two-dimensional (2D) materials carry momentum large enough to approach the momenta of electrons in solids. Consequently, they enable tunable control over the absorption and emission frequencies in solids

without altering their intrinsic electronic properties. In particular, we analyse a graphene monolayer supporting plasmon polaritons adjacent to a GaAs/InGaAs/GaAs quantum well (QW) and consider the QW intersubband transitions (Fig. 1a). We obtain tunable frequency shifts on the order of tens to hundreds of meV in the spectrum of the emitted and absorbed polaritons, as well as substantial rate enhancements.

Increasing the momentum of photons through polaritonic materials and approaching the range of electron momenta in solids is expected to break one of the most basic notions in optics—that the optical material response is local. Optical transitions facilitated by free-space photons are nearly direct due to their small momentum: as a consequence, the associated energy change of the transitioning electron is fixed by the photon frequency, while its momentum change is negligible. As a result, the transition dynamics of the electron can be accurately captured by a local dielectric function that depends only on the transition frequency  $\omega$  and is independent of the photon momentum. In contrast to this, several studies have revealed the breakdown of the local paradigm in deeply nanoscopic plasmonic structures<sup>17–20</sup>, whose behaviour necessitates an account of the material non-local response (generally described by the spatial dispersion of  $\epsilon(\mathbf{r}, \mathbf{r}', \omega)$ ), which includes two space coordinates  $\mathbf{r}, \mathbf{r}'$ ). In translationally invariant systems, where  $\epsilon(\mathbf{r}, \mathbf{r}', \omega) = \epsilon(\mathbf{r} - \mathbf{r}', \omega)$ , the non-local response is equivalent to an explicit momentum ( $\mathbf{q}$ ) dependence of the dielectric function, that is,  $\epsilon(\mathbf{q}, \omega)$ <sup>21–25</sup>. Recent experiments probing intrinsic non-localities in graphene plasmonics<sup>26</sup> and effective non-localities in metamaterials<sup>27</sup> further highlight the emerging primacy of non-locality. An intriguing question related to these observations is whether it is possible to ‘induce’ a non-local response or control the intrinsic non-locality of a material by coupling it to an adjacent polaritonic material.

We find that the QW exhibits a pronounced non-local response when interacting with the large-momentum polariton (the optical field), despite the fact that each system, considered separately, can be accurately described by a local optical response. The coupled system thus enters a qualitatively new light–matter interaction

<sup>1</sup>Department of Electrical Engineering, Technion, Israel Institute of Technology, Haifa, Israel. <sup>2</sup>Department of Physics, Massachusetts Institute of Technology, Cambridge, MA, USA. \*e-mail: [skurman@campus.technion.ac.il](mailto:skurman@campus.technion.ac.il); [kaminer@technion.ac.il](mailto:kaminer@technion.ac.il)

regime beyond the local optical response and therefore also beyond the dipole approximation. We find two particularly interesting manifestations of this non-locality: a Doppler effect for emission and absorption frequencies, and an intrinsic cutoff frequency for absorption. The platform proposed in this work enables several new opportunities in both fundamental and applied sciences: at a fundamental level, the controlled study of basic conceptual questions in non-locality; at an applied level, opportunities ranging from improved solar cells, enabled by broader absorption spectra, to tunable solid-state LEDs and lasers, enabled by an effectively tunable bandgap.

## Results

**Theory of graphene-QW interactions.** The system of interest, sketched in Fig. 1a, is a QW of thickness  $d$  that may emit or absorb a plasmon, confined to an adjacent graphene layer, which, in turn, is separated from the QW active area by a spacer of thickness  $l_s = 10$  nm. The graphene sheet supports plasmons of momenta far greater than that of free-space photons (Fig. 1b): consequently, these plasmons enable non-vertical transitions between electronic subbands of the QW (indicated as solid black lines in Fig. 1b). We will now describe the physical properties of each of these individual components as well as the required characteristics for their interactions.

The graphene layer is the propagation medium of the graphene plasmons, whose electromagnetic field dominates the optical interaction with the QW. The electromagnetic field of a graphene plasmon is a highly confined evanescent wave supported by the sloshing of charge density in the graphene sheet. Graphene plasmons are especially attractive for our purpose thanks to the versatility of graphene's conductivity and Fermi level (adjustable via chemical or electrical doping in the graphene layer)<sup>28–30</sup>, as well as its potentially low-loss extreme light confinement, that is, wavelength shrinkage to lengths hundreds of times smaller than that of a free-space photon<sup>26,31–33</sup>. The confinement factor, defined as  $\eta_0 = c/v_p = \lambda_0/\lambda_{p1}$ , represents in dimensionless terms the reduced plasmon phase velocity  $v_p$  relative to the speed of light in vacuum  $c$ , or, equivalently, the reduced plasmon wavelength  $\lambda_{p1}$  relative to the free-space value  $\lambda_0$ .

In this Article, we exploit a hallmark of graphene plasmonics, namely that  $\eta_0$  can greatly exceed unity<sup>26,33,34</sup>. Consequently, an electric field mode  $\mathbf{E}_q$  of a plasmon confined to the  $x$ - $y$  plane with wavevector  $\mathbf{q}$  (momentum  $\hbar\mathbf{q}$ ) can be simplified to

$$\mathbf{E}_q(\mathbf{r}) \propto e^{-q|z|} e^{-iq \cdot \boldsymbol{\rho}} (\hat{\mathbf{q}} \pm i\hat{\mathbf{z}}) \quad (1)$$

where  $\boldsymbol{\rho}$  is the position in the  $x$ - $y$  plane. The graphene plasmon dispersion relation can be expressed within the intraband approximation (that is, by a Drude-like model, see Methods) with intrinsic decay time of  $\tau = 0.2$  ps (ref. 29):

$$\omega_q \simeq \sqrt{\frac{4\alpha}{\epsilon_s + 1} \frac{E_F^g}{\hbar}} cq = v_p(q)q \equiv \frac{cq}{\eta_0(q)} \quad (2)$$

where  $\epsilon_s$  is the spacer permittivity (taken to be 10.6 for GaAs),  $\alpha$  is the fine-structure constant and  $\hbar$  is the reduced Planck constant.  $E_F^g$  is the graphene Fermi level, which can be tuned by electrostatic gating or chemical doping to control the confinement factor and the plasmon dispersion.

Representing the dispersion through the (momentum-dependent) confinement factor  $\eta_0(q)$  allows a direct extension of the key concepts discussed here to any surface polaritonic system (for example, phonon polaritons<sup>35–37</sup>, other families of polaritons<sup>38,39</sup> and their heterostructures<sup>33,40</sup>), all of which can be used to realize the results presented in this work. An important challenge pertinent to all of these high-confinement polaritons is the need to

couple the polaritons in or out of the supporting material. Various methods facilitate such coupling: for example, plasmons hosted by the graphene sheet can be coupled out by a scanning near-field optical microscopy (SNOM) tip<sup>31</sup> or by a periodic grating<sup>41,42</sup>; alternatively, they could be emitted or absorbed by any nearby quantum emitter, constrained only by the conservation of energy and momentum (Fig. 1b).

We demonstrate the emission and absorption of plasmons with a 12 nm GaAs/InGaAs/GaAs QW, wide enough to support three electron subbands. Control over the energy distribution of the QW electrons can be accomplished by electrical, optical or chemical doping. The distribution of the electrons is described by an effective temperature  $T_{\text{eff}}$  and a QW quasi Fermi level  $E_F^{\text{QW}}$  (as described in ref. 43), which are a function of the electronic excitation mechanism (for example, the frequency and power of the driving laser in the case of optical excitation), and depend also on different charge relaxation rates. Under standard parameters, a simple single-particle treatment has the following energies and wavefunctions of the charge carriers:

$$E_{nk} = E_n + \frac{\hbar^2 \mathbf{k}^2}{2m^*} \quad (3a)$$

$$\psi_{nk}(\mathbf{r}) = e^{-ik \cdot \boldsymbol{\rho}} \phi_n(z - z_0) \quad (3b)$$

with  $n = 1, 2, 3$  for the three QW electron subbands.  $E_n$  and  $\phi_n(z)$  represent the QW energy minima and out-of-plane wavefunction<sup>44</sup> (Fig. 1a),  $z_0$  is the location of the QW centre, and  $m^*$  is the effective mass of charge carriers.  $\mathbf{k}$  is the electron wavevector in the  $x$ - $y$  plane, in which the charge carriers behave like a 2D free electron gas, resulting in parabolic subbands.

The coupling between plasmons and the QW charge carriers can be described by macroscopic quantum electrodynamics (originally discussed in the context of atomic systems, for example, refs 34,45–47). The key steps are presented in the following, and additional technical details are provided in Supplementary Section 1. The electron-photon interaction is governed by the interaction Hamiltonian (in the Weyl gauge, that is, with zero scalar potential):

$$H_{\text{int}} = \frac{e}{2m^*} [\mathbf{p} \cdot \mathbf{A}(\mathbf{r}) + \mathbf{A}(\mathbf{r}) \cdot \mathbf{p}] \quad (4a)$$

$$A_i(\mathbf{r}) = \sqrt{\frac{\hbar}{\pi\epsilon_0}} \int d\omega \frac{\omega}{c^2} \int d\mathbf{r}' \sqrt{\text{Im}[\epsilon(\mathbf{r}', \omega)]} \hat{f}_i(\mathbf{r}, \mathbf{r}', \omega) + \text{h. c.} \quad (4b)$$

where  $e$  is the QW carrier's charge,  $\mathbf{p}$  its momentum operators, and  $\mathbf{A}$  is the vector potential operator of the electromagnetic field. The field quantization of the vector potential follows by expansion in annihilation (creation) operators  $\hat{f}_i(\mathbf{r}', \omega)$  ( $\hat{f}_i^\dagger(\mathbf{r}', \omega)$ ) that describe a dipole excitation at position  $\mathbf{r}'$ , with frequency  $\omega$ , and direction  $j$ . The vector potential operator incorporates details of the optical environment (for example, knowledge of the supported plasmon modes) through the imaginary part of the permittivity  $\epsilon$  and the dyadic Green's function  $\mathbf{G}(\mathbf{r}, \mathbf{r}', \omega)$ . The dyadic Green's function components  $G_{ij}(\mathbf{r}, \mathbf{r}', \omega)$  represent the  $i$ th component of the electromagnetic field at position  $\mathbf{r}$  due to a time-harmonic point dipole at position  $\mathbf{r}'$  oriented along the  $j$ th direction. An explicit expression for the Green's function of the system under consideration is given in Supplementary equation (2).

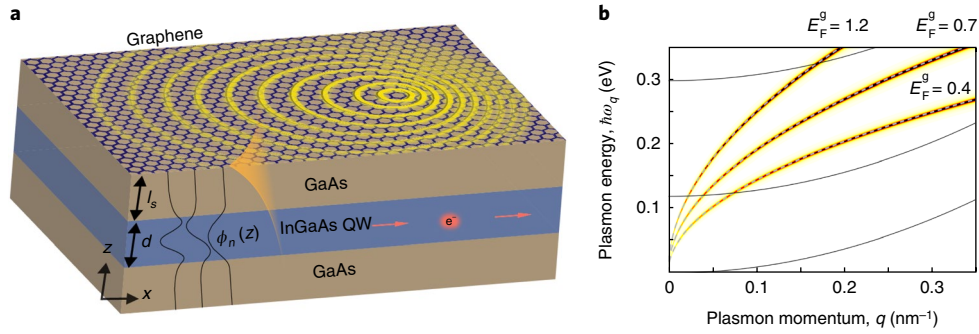


**Fig. 1 | Illustration of the coupling of graphene plasmon polaritons to a quantum well.** **a**, Scheme of the structure. A graphene layer is situated above the QW. Plasmon polariton wavefronts supported by the graphene layer are illustrated by yellow waves. The  $z$  profiles of the QW eigenmodes  $\phi_n(z)$  (black) and of the plasmon field (yellow) are illustrated on the left. **b**, Plasmon dispersion for the structure in **a** for graphene Fermi levels of 0.4, 0.7 and 1.2 eV. The colourmap presents the imaginary part of the reflection coefficient using the local random phase approximation model<sup>28</sup>, overlaid with the Drude model dispersion curves (dashed lines). The match between the curve and the colourmap demonstrates the Drude model validity. QW electronic subbands are shown in black: the large plasmonic momenta enable non-vertical transitions between QW subbands. For example, an electron initially at rest can undergo transitions corresponding to the intersections between the plasmonic and QW dispersions.

The use of the dyadic Green’s function allows a full account of the impact of intrinsic material losses. The impact of losses are incorporated in the spatial Fourier transformed  $\mathbf{G}(\mathbf{q}, \omega)$ , whose amplitude is proportional to the imaginary part of the reflectance (plotted in Fig. 1b), and therefore incorporates the plasmonic dispersion (equation (2)) and broadening. Furthermore, the Green’s function also comprises the full spatial dependence of the mode  $e^{-iq \cdot \rho - q|z|}$ , which in our case includes the full momentum dependence  $e^{-iq \cdot \rho}$  along the QW extended direction, and consequently goes beyond the dipole approximation that is unjustified in our settings. For this reason, we enter a regime that enables non-vertical transitions in the QW dispersion diagram, as shown in Fig. 2a,b. We see that the full exploitation of the polaritonic momentum in electronic transitions is attainable in non-atomic, extended emitters, such as QWs.

**Transition frequency shift due to plasmon momentum.** In this section we analyse the transition spectra of plasmons emitted or absorbed by the QW and show how the large plasmon momentum alters the QW transition frequencies. The first step is to look at the transition rate between QW states due to the emission (em) or absorption (ab) of a plasmon in the considered structure. In this structure, the transition rates fall within the weak coupling paradigm; strong coupling will only become potentially relevant for sub-nanometre spacers. Hence, it is justified to obtain the rates directly from Fermi’s golden rule<sup>48</sup>:

$$\Gamma_{ab}^{em} = \frac{2\pi}{\hbar} \sum_{\mathbf{k}_i, \mathbf{k}_f} \left| \langle n_f, \mathbf{k}_f, n_q \pm 1 | H_{int} | n_i, \mathbf{k}_i, n_q \rangle \right|^2 f(\mathbf{k}_i) \delta(E_{n_i, \mathbf{k}_i} - E_{n_f, \mathbf{k}_f} \mp \hbar\omega_q) \quad (5)$$

where

$$f(\mathbf{k}_i) = \left( 1 + \exp \left[ \left( \frac{\hbar^2 k_i^2}{2m^*} - E_F^{QW} \right) / k_B T_{eff} \right] \right)^{-1}$$

is the Fermi–Dirac distribution as a function of an electronic momentum  $\hbar\mathbf{k}_i$  and the final state is assumed to be vacant. Subscripts  $i$  and  $f$  denote the initial and final states of the electron, while  $n_q$  is the number of plasmon quanta (increased/decreased for emission/absorption). Although the calculation can be done for any  $n_q$ , for simplicity we focus on the cases where  $n_q=0$  when considering

spontaneous plasmon emission and  $n_q=1$  when considering plasmon absorption. The results presented are normalized to yield transition rates per charge carrier, that is, such that  $1 = \frac{A}{(2\pi)^2} \int d\mathbf{k}_i f(\mathbf{k}_i)$  for a slab of area  $A$ .

The matrix element in equation (5) that specifies the interaction amplitude between graphene plasmons and the QW is approximately given by (Supplementary Section 1)

$$\frac{\langle n_f, \mathbf{k}_f, n_q \pm 1 | H_{int} | n_i, \mathbf{k}_i, n_q \rangle}{\langle n_f | e^{-qz} | n_i \rangle} \frac{\langle \mathbf{k}_f | e^{\pm iq \cdot \rho} | \mathbf{k}_i \rangle}{\langle \mathbf{k}_f | e^{\pm iq \cdot \rho} | \mathbf{k}_i \rangle} \quad (6)$$

The first term (i) gives the  $z$ -dependent interaction amplitude due to overlap between the evanescent tail of the plasmon and the charge carrier state inside the QW (Fig. 1a), where the  $\partial_z$  derivative arises from the momentum operator. Term (ii) ensures momentum conservation in the  $x$ - $y$  plane, forcing  $\mathbf{k}_i \pm \mathbf{q} = \mathbf{k}_f$ , which appears as a delta function in the lossless case or a Lorentzian when including plasmonic losses. Meanwhile, the frequency-dependent delta function,  $\delta(E_{n_i, \mathbf{k}_i} - E_{n_f, \mathbf{k}_f} \mp \hbar\omega_q)$  in equation (5), enforces energy conservation. The allowed transition frequencies associated with the emission or absorption of a plasmon are consistent with the combined energy–momentum conservation, and can be determined by substituting the dispersion relations of both the plasmon and the QW electron, equations (2) and (3a), into these conservation laws. Figure 2a,b illustrates the tunable transition frequencies that follow from these conservation laws (for an electron initially at rest), with the tunability courtesy of the gate-tunable plasmon dispersion.

Figure 2c–f displays the tunability in the transition frequencies when increasing the momentum of the plasmon, as expected from Fig. 2a,b. Specifically, the absorption and emission frequencies show blue- and redshifts, respectively, breaking the symmetry between them with a split as wide as 100 meV. Comparing the panels in Fig. 2c–f illustrates how the frequency shifts increase as the Fermi level of graphene decreases, which corresponds to increasing the plasmon momentum, that is, increasing the confinement factor. In addition to a frequency shift, the QW transitions also exhibit spectral broadening due to plasmonic losses, with an increase in the full-width at half-maximum (FWHM) of the spectral lines of up to 10 meV, which will be further broadened as discussed below by a Doppler broadening effect. The broadening of the FWHM could be

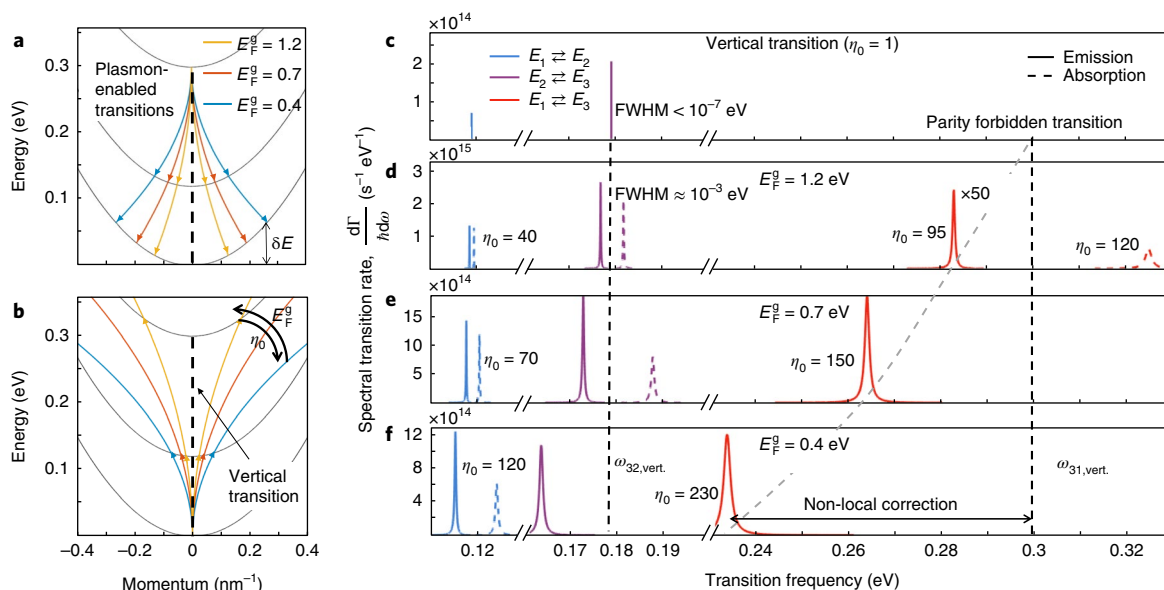


**Fig. 2 | Control of the emission and absorption frequencies of a quantum well by tuning the graphene Fermi energy.** **a, b**, Concept of the controllable transition frequencies. Plasmonic emission (**a**) and absorption (**b**) between the QW subbands (black) for different graphene Fermi levels (blue,  $E_F^g = 0.4$  eV; red,  $0.7$  eV; yellow,  $1.2$  eV). The transition frequency shift is marked by  $\delta E$ . **c–f**, Total rates of emission (solid) and absorption (dashed) per charge carrier of the different transitions (blue,  $E_1 \rightleftharpoons E_2$ ; purple,  $E_2 \rightleftharpoons E_3$ ; red,  $E_1 \rightleftharpoons E_3$ ) for several values of the graphene Fermi level when the electron is initially at the bottom of the subband. Confinement factors of the corresponding transitions are indicated. Dashed black lines represent the local-response resonance frequencies (that is, vertical transitions), and the grey dashed line is a guide to the eye for emphasizing the non-local frequency shift.

understood through Fig. 1b from the width of the plasmonic dispersion and its intersection with the electronic dispersion line.

In line with previous findings<sup>49,50</sup>, Fig. 2 also shows that the total transition rates (the integrated spectra) are significantly enhanced for an interaction with plasmons that have large confinement factors ( $\eta_0$ ). As a result of the large Purcell factor, we find that the radiative plasmon transitions dominate all other radiative processes (Supplementary Fig. 5), such as QW emission into free-space photons. In contrast with previous findings, Fig. 2 shows that there is a difference between the absorption rate and the emission rate. This change in spectral response between absorption and emission, and the large change compared to the local response (that is, vertical transitions) plotted in Fig. 2a,b, underscore the impact of the induced non-locality in the QW response. Moreover, we find that the spacer thickness affects the enhancement of all transitions, and limits the range of confinement factors that enhance the transitions. The reason lies in the fact that large confinements shorten the plasmon tail in the  $z$  direction to a characteristic length of  $\frac{c}{\eta_0 \omega_q}$ , as seen in equation (6) term (i) (for more details see Supplementary Fig. 8).

Figure 3 summarizes the large dependence of the absorption frequencies, emission frequencies and transition rates of distinct intersubband transitions on the plasmon confinement factor. In this representation, the gradual change from the free-space photon transition rates and spectra ( $\eta_0 = 1$ ) to the high momentum plasmon transition rates and spectra (that is, high values of  $\eta_0$ ) is apparent. The first notable feature in Fig. 3 is the strong enhancement of transition  $E_1 \rightleftharpoons E_3$ , which due to the parity symmetry of the wavefunctions, has a vanishing dipole moment but a non-vanishing quadrupole moment in the  $z$  direction. In the absence of coupling to plasmons, this transition is much slower than the  $E_1 \rightleftharpoons E_2$  transition on account of the weak variation of the electromagnetic field that practically forbids any beyond-dipole transition in the QW. However, in the presence of plasmons, the  $E_1 \rightleftharpoons E_3$  transition can be enhanced by up to seven orders of magnitude (here achieved for a confinement factor of 85). This transforms the  $E_1 \rightleftharpoons E_3$  transition from effectively forbidden

to one with a rate exceeding even the conventional, non-forbidden transitions (for example,  $E_1 \rightleftharpoons E_2$ ) of the QW. Interestingly, we find that the rates of both kinds of transition are not merely influenced by the out-of-plane fields and field gradients; they are also strongly influenced by the in-plane plasmon momentum, which emphasizes the importance of the complete non-local description. The solid black lines in Fig. 3a present a comparison with the conventional local calculation of the transition rates, where we neglect the finite plasmon momentum by approximating  $e^{iq \cdot p} \approx 1$  in equation (6) that yields a conventional dipole  $\mathbf{d} \cdot \mathbf{E}$  interaction term. The deviation between the curves in Fig. 3a shows that the local calculation fails for the  $E_1 \rightleftharpoons E_3$  transition even at relatively low confinements, further underscoring the importance of going beyond the dipolar approximation (for further details see Supplementary Section 6).

Another interesting effect revealed by rigorously accounting for the large plasmon momenta is the appearance of a cutoff confinement factor  $\eta_{0,co}$  (or, equivalently, a cutoff Fermi level) for the QW absorption (Fig. 3b). In particular, above this confinement there are no absorptive transitions that satisfy the conservation of energy and momentum laws previously discussed. The reason is straightforward and immediately appreciable from Fig. 2b: at sufficiently low Fermi levels, the plasmon dispersion bends so rapidly that it ‘misses’ its intersection with the next subband (inset in Fig. 3b). For an electron initial at rest, we obtain a closed-form expression for the cutoff graphene Fermi level

$$E_{F,co}^g = \frac{\epsilon_s + 1}{\alpha} \frac{\left(\frac{2}{3} \Delta E\right)^{3/2}}{\sqrt{m^* c^2}}$$

where  $\Delta E = E_{n_r,0} - E_{n_l,0}$  is the QW energy level difference. Interestingly, the cutoff Fermi level corresponds to a maximum confinement factor

$$\eta_{0,co} = \frac{3}{8} \frac{\hbar \omega_q}{\Delta E} \sqrt{\frac{3m^* c^2}{2\Delta E}}$$

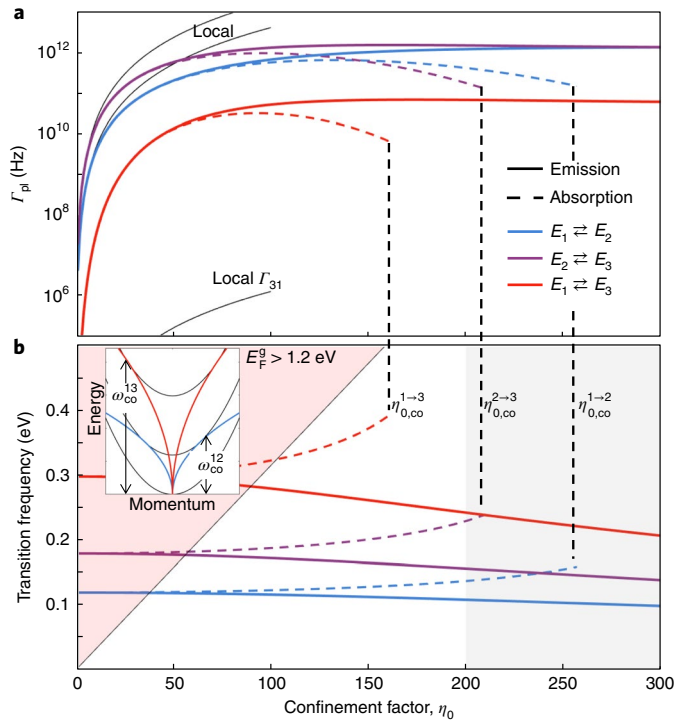


**Fig. 3 | Confinement factor effect on plasmonic transitions.** **a, b**, Transition rates **(a)** and frequencies **(b)** as a function of plasmon confinement factor (dashed lines, absorption; solid lines, emission) for the three possible transitions (blue,  $E_1 \rightleftharpoons E_2$ ; purple,  $E_2 \rightleftharpoons E_3$ ; red,  $E_1 \rightleftharpoons E_3$ ). The corresponding local calculation is shown in black (equal for absorption and emission). In **b**, the red shaded area marks graphene Fermi level above 1.2 eV, and the grey shaded area marks confinements where the Drude model fails. Inset in **b**: QW subbands overlaid by the plasmon dispersion for two absorption transitions, with the Fermi levels having cutoff values  $E_F^g = E_{F,co}^g$  for the second and third subbands. All curves are for the plasmonic lossless case, with a single electron initially at rest ( $k_i = 0$ ). For the same plots as a function of  $E_F^g$ , see Supplementary Fig. 7.

which is found within experimental range thanks to a combination of the electron’s small effective mass and the graphene’s large confinement factor. When  $E_F^g < E_{F,co}^g$ , absorption between the two relevant subbands is forbidden in any frequency, and when  $E_F^g > E_{F,co}^g$ , the absorption channels open (where the higher frequency absorption channel is significantly slower; Supplementary Fig. 5). In the same spirit, additional absorption channels are likely to exist at higher frequencies due to other intersubband transitions beyond the parabolic band approximation.

To further investigate the frequency shift due to the plasmon’s momentum, we examine the transitions of a charge carrier not initially at rest ( $\mathbf{k}_i \neq 0$ ) and reveal a Doppler effect. We denote the angle  $\theta$  between a plasmon at direction  $\hat{\mathbf{q}}$  and the direction of the initial momentum of the charge carrier  $\hat{\mathbf{k}}_i$ , so that  $\theta = \arccos(\hat{\mathbf{k}}_i \cdot \hat{\mathbf{q}})$ . Figure 4a shows that for the case of plasmon emission, when  $\theta$  varies from 0 to  $\pi$ , the plasmon frequency can vary by tens of meV. Consequently, the distribution of charge carriers in the QW (that is, distribution in  $k_i$ ) alters the frequency bandwidth of each QW transition. We now explain this behaviour analytically as a manifestation of a Doppler shift.

According to the Doppler shift, a moving charge observes waves with a shifted frequency that depends on the relative angle  $\theta$  (as defined in the previous paragraph). Importantly, the conventional Doppler effect carries the hidden assumption that the charge momentum is unchanged by the interaction with the wave. The Doppler shift in our case is different from the conventional one

because the momentum of the charge can change significantly during the interaction with the plasmon (inset of Fig. 4a); that is, the recoil of the charge carrier alters the conventional Doppler formula. As expected, the recoil is negligible for low confinement factors (and low plasmon momentum), so that the transition rates are angle-independent, and the transition frequencies follow the conventional Doppler formula:

$$\omega_q(\theta) = \omega_q(\pi/2) \left( 1 - \frac{v_i \cos(\theta)}{v_p(q)} \right)^{-1} \quad (7)$$

where  $\omega_q(\theta)$  represents the frequency of the plasmon emission/absorption for a specific angle of emission or absorption. The charge carrier velocity is  $v_i$  and the plasmon phase velocity is  $v_p(q)$ . Equation (7) reveals not only the angle dependence of the frequency but also the graphene Fermi energy dependence, because it controls the plasmon phase velocity. Although equation (7) takes the form of a conventional Doppler shift, we find that for high confinement factors, the recoil of the charge carrier can cause substantial deviations from the conventional Doppler shift, leading to a recoil-dependent generalized Doppler shift alongside highly angle-dependent transition rates (Supplementary Fig. 9).

Figure 4b,c presents a Doppler broadening of the emission and absorption spectra for transitions between the first and second electronic subbands, for three different graphene Fermi levels  $E_F^g$  and two effective temperatures, calculated by integrating over  $k_i, \theta$  (equation (5)). Although the known Doppler broadening expression agrees with the results for low confinement factors (Supplementary Section 3), in high confinement factors the inhomogeneous transition rates in the Doppler effect cause the overall peak to be redshifted, as demonstrated in Fig. 4c and its inset. Despite the broadening, at low temperatures (Fig. 4b) the separation between the peaks of emission and absorption is observable, with a split exceeding 10 meV for  $E_F^g < 0.7$  eV.

We conclude our discussion of the Doppler shift by noting that the Doppler effect in the system is itself a manifestation of non-locality, as previously noted by, for example, Landau and Lifschitz<sup>31</sup>: the frequency and rate of plasmon absorption is explicitly dependent on the plasmon wavevector through the angle of absorption  $\theta$ . Because the absorption rate is directly proportional to the imaginary part of the dielectric function,  $\Gamma \propto \text{Im } \epsilon(\mathbf{q}, \omega)$ , it follows that the QW permittivity is wavevector dependent and therefore spatially non-local.

**Discussion**

To summarize, we have demonstrated that the large momenta of surface polaritons can be used to control the frequencies of polaritons emitted or absorbed by electrons in a solid-state emitter. Specifically, the combination of a QW and a plasmon supporting monolayer of graphene enables substantial control over the spectral properties of the system, through graphene’s tunable Fermi level. The full transition dynamics manifests new effects such as an absorption cutoff and pronounced Doppler shifts that suggest intriguing possibilities, such as bound electron acceleration (Supplementary Section 7). This control of the transition spectrum also enables tuning of the intrinsic optical response and the effective permittivity of the system (because  $\Gamma \propto \text{Im } \epsilon(\mathbf{q}, \omega)$ ), spanning over twentyfold when the wavevector and the frequency fulfil the plasmonic dispersion relations (Supplementary Section 5 and Supplementary Fig. 2). As a result, our work suggests a framework for designing new, tunable, non-local metamaterials from local constituents.

The scheme introduced in this Article can be generalized to a host of surface polariton systems interfaced with various solid-state emitters simply by substituting the material properties of the polaritons and electrons, that is, their dispersions. Other 2D materials

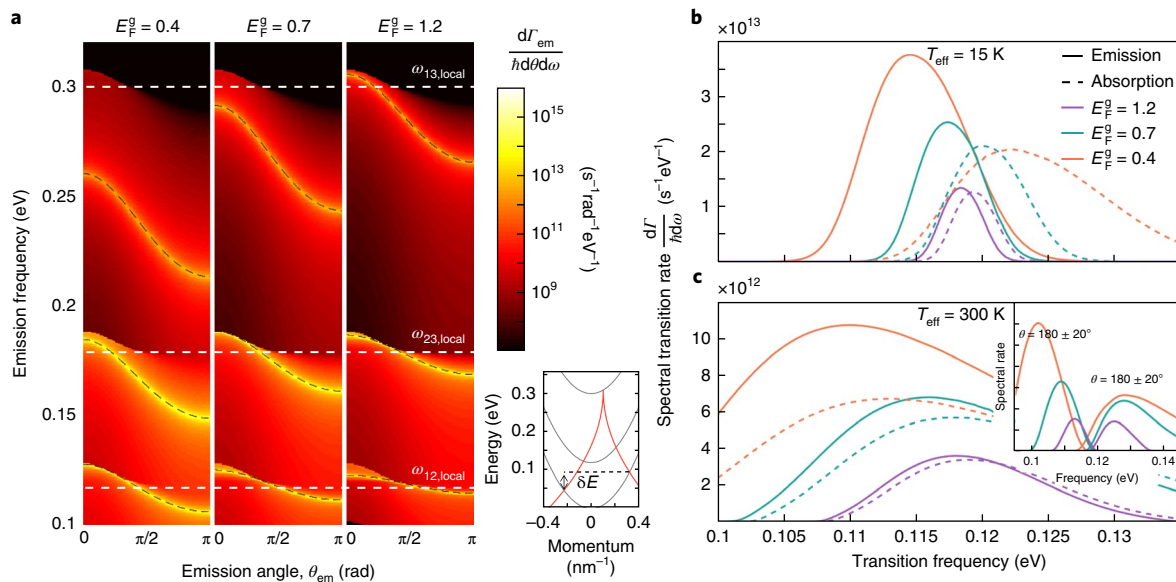


**Fig. 4 | Doppler effect in plasmonic transitions.** **a**, Angular spectral emission rate for an electron with initial momentum of  $k_i = 0.1 \text{ nm}^{-1}$  and three graphene Fermi level energies  $E_F^g = 0.4, 0.7$  and  $1.2 \text{ eV}$ , illustrating the sharp break with the local description (dashed white lines). Black dashed lines present emission frequencies according to our lossless formula that generalizes the conventional Doppler shift, showing a good match with full Green's function simulations. Inset: QW band diagram and possible transitions to opposite directions for a non-zero initial electron momentum  $\mathbf{k}$ , showing the direction-dependent Doppler frequency shift marked by  $\delta E$ . **b, c**, Spectral emission (solid lines) and absorption (dashed lines) rates for several graphene Fermi level values for the  $E_1 \rightleftharpoons E_2$  transition when the effective temperature of the electrons in the QW is  $T_{\text{eff}} = 15 \text{ K}$  (**b**) and  $300 \text{ K}$  (**c**), where the quasi-Fermi level is  $1.5 \text{ meV}$  above the bottom of the initial subband. Inset: spectral emission rates forward in angles  $0 \pm 20^\circ$  and backward in angles  $180 \pm 20^\circ$ .

and polar dielectric structures supporting phonon polaritons, such as hexagonal boron nitride, offer several interesting opportunities in this regard. For example, the highly frequency-selective nature of phonon polaritons<sup>35–37</sup> may enable additional spectral control over the QW intersubband transitions in addition to the strong enhancements of light–matter interactions offered by such materials<sup>49</sup>. The formalism can also be generalized to intersubband transitions in other QW structures such as in few-layer transition-metal dichalcogenides<sup>52</sup> and narrow-bandgap materials<sup>53</sup>, as well to interband transitions in these materials and in others. Further still, the formalism could be extended to cascade processes in multi-level systems as in ref. <sup>54</sup>, thus capturing the complete dynamics of the QW electrons when experiencing multiple consecutive transitions. The limit of our formalism is the strong coupling regime that might occur when a spacer of few atomic layers separates the electronic states and the plasmons, leading to the formation of a new type of polariton composed of the QW intersubband polariton and the graphene plasmon (potentially accompanied by a Lamb-shift-type frequency shift<sup>55</sup>).

The ability to access very large electromagnetic field momenta could also affect the optical response of indirect-bandgap bulk semiconductors<sup>56,57</sup>, which are typically constrained in their inability to interact with light near their indirect bandgap due to the large electronic momentum mismatch between valence maximum and conduction minimum. Coupling such materials to a polariton-supporting 2D layer could conceivably provide the momentum necessary to overcome this mismatch—even without altering its electronic band structure (for example, by introducing defects). A proof of concept can be implemented using multi-layer MoSe<sub>2</sub> as an emitter, which has been found to change from direct to indirect depending on the number of layers<sup>58,59</sup>, making this material an ideal candidate for such an experimental proof of concept (potentially in a heterostructure with adjacent polariton-supporting 2D materials). A particularly exciting realization of this idea would be inducing indirect-bandgap transitions in

silicon, a material of extreme technological importance. To cross the Brillouin zone with a high-momentum polariton, one would typically still want to modify the electronic structure (for example, with porous silicon<sup>60</sup>). With a combination of band structure engineering and large-momenta polaritons, one could envision designing more efficient silicon solar cells, silicon photodetectors and silicon-based light sources. Such devices, which could be integrated on a chip easily, would greatly contribute to creating simple, robust hybrid electronic–photonic systems.

## Methods

Methods, including statements of data availability and any associated accession codes and references, are available at <https://doi.org/10.1038/s41566-018-0176-6>.

Received: 27 November 2017; Accepted: 19 April 2018;

Published online: 4 June 2018

## References

1. Yariv, A. *Quantum Electronics* 3rd edn (Wiley, New York, NY, 1989).
2. Schubert, E. F. *Light Emitting Diodes* (Cambridge Univ. Press, Cambridge, 2006).
3. Theuwissen, A. J. P. *Solid-State Imaging with Charge-Coupled Devices* Vol. 1 (Kluwer Academic, Boston, MA, 1995).
4. Green, M. A. *Solar Cells: Operating Principles, Technology and System Applications* (Univ. New South Wales, Sydney, 1998).
5. Purcell, E. M. Spontaneous emission probabilities at radio frequencies. *Phys. Rev.* **69**, 681–681 (1946).
6. Kleppner, D. Inhibited spontaneous emission. *Phys. Rev. Lett.* **47**, 233–236 (1981).
7. Pelton, M. Modified spontaneous emission in nanophotonic structures. *Nat. Photon.* **9**, 427–435 (2015).
8. Vats, N., John, S. & Busch, K. Theory of fluorescence in photonic crystals. *Phys. Rev. A* **65**, 043808 (2002).
9. Neogi, A. et al. Enhancement of spontaneous recombination rate in a quantum well by resonant surface plasmon coupling. *Phys. Rev. B* **66**, 153305 (2002).
10. Lamb, W. E. & Retherford, R. C. Fine structure of the hydrogen atom by a microwave method. *Phys. Rev.* **72**, 241–243 (1947).
11. Bethe, H. A. The electromagnetic shift of energy levels. *Phys. Rev.* **72**, 339 (1947).

12. Wylie, J. M. & Sipe, J. E. Quantum electrodynamics near an interface. *Phys. Rev. A* **30**, 1185–1193 (1984).
13. Khitrova, G., Gibbs, H. M., Kira, M. S., Koch, W. & Scherer, A. Vacuum Rabi splitting in semiconductors. *Nat. Phys.* **2**, 81–90 (2006).
14. Zhang, Y. et al. Sub-nanometre control of the coherent interaction between a single molecule and a plasmonic nanocavity. *Nat. Commun.* **8**, 15225 (2017).
15. Chang, C. H., Rivera, N., Joannopoulos, J. D., Soljačić, M. & Kaminer, I. Constructing 'designer atoms' via resonant graphene-induced lamb shifts. *ACS Photon.* **4**, 3098–3105 (2017).
16. Cohen-Tannoudji, C., Dupont-Roc, J. & Grynberg, G. *Photons and Atoms: Introduction to Quantum Electrodynamics* (Wiley, New York, NY, 1989).
17. Scholl, J. A., Koh, A. L. & Dionne, J. A. Quantum plasmon resonances of individual metallic nanoparticles. *Nature* **483**, 421–427 (2012).
18. Raza, S. et al. Blueshift of the surface plasmon resonance in silver nanoparticles studied with EELS. *Nanophotonics* **2**, 131–138 (2013).
19. Jin, D. et al. Quantum-spillover-enhanced surface-plasmonic absorption at the interface of silver and high-index dielectrics. *Phys. Rev. Lett.* **115**, 193901 (2015).
20. Raza, S. et al. Multipole plasmons and their disappearance in few-nanometre silver nanoparticles. *Nat. Commun.* **6**, 8788 (2015).
21. Raza, S., Bozhevolnyi, S. I., Wubs, M. & Mortensen, N. A. Nonlocal optical response in metallic nanostructures. *J. Phys. Condens. Matter* **27**, 183204 (2014).
22. Christensen, T. *From Classical to Quantum Plasmonics in Three and Two Dimensions* (Springer, New York, NY, 2017).
23. Varas, A., Garcia-Gonzalez, P., Feist, J., Garcia-Vidal, F. J. & Rubio, A. Quantum plasmonics: from jellium models to ab initio calculations. *Nanophotonics* **5**, 409–426 (2016).
24. Zhu, W. et al. Quantum mechanical effects in plasmonic structures with subnanometre gaps. *Nat. Commun.* **7**, 11495 (2016).
25. Fitzgerald, J. M., Narang, P., Craster, R. V., Maier, S. A. & Giannini, V. Quantum plasmonics. *Proc. IEEE* **104**, 2307–2322 (2016).
26. Lundberg, M. et al. Turning quantum non-local effects in graphene plasmonics. *Science* **357**, 187–191 (2017).
27. Ginzburg, P. et al. Spontaneous emission in non-local materials. *Light Sci. Appl.* **6**, e16273 (2017).
28. Garcia de Abajo, F. J. Graphene plasmonics: challenges and opportunities. *ACS Photon.* **1**, 135–152 (2014).
29. Jablan, M., Buljan, H. & Soljačić, M. Plasmonics in graphene at infrared frequencies. *Phys. Rev. B* **80**, 245435 (2009).
30. Jablan, M., Soljačić, M. & Buljan, H. Plasmons in graphene: fundamental properties and potential applications. *Proc. IEEE* **101**, 1689–1704 (2013).
31. Chen, J. et al. Optical nano-imaging of gate-tunable graphene plasmons. *Nature* **487**, 77–81 (2012).
32. Fei, Z. et al. Gate-tuning of graphene plasmons revealed by infrared nano-imaging. *Nature* **487**, 82–85 (2012).
33. Woessner, A. et al. Highly confined low-loss plasmons in graphene–boron nitride heterostructures. *Nat. Mater.* **14**, 421–425 (2014).
34. Rivera, N., Kaminer, I., Zhen, B., Joannopoulos, J. D. & Soljačić, M. Shrinking light to allow forbidden transitions on the atomic scale. *Science* **353**, 263–269 (2016).
35. Hillenbrand, R., Taubner, T. & Keilmann, F. Phonon-enhanced light–matter interaction at the nanometre scale. *Nature* **418**, 159–162 (2002).
36. Taubner, T., Korobkin, D., Urzhumov, Y., Shvets, G. & Hillenbrand, R. Near-field microscopy through a SiC superlens. *Science* **313**, 1595 (2006).
37. Dai, S. et al. Tunable phonon polaritons in atomically thin van der Waals crystals of boron nitride. *Science* **343**, 1125–1129 (2014).
38. Basov, D. N., Fogler, M. M. & Garcia de Abajo, F. J. Polaritons in van der Waals materials. *Science* **354**, aag1992 (2016).
39. Low, T. et al. Polaritons in layered two-dimensional materials. *Nat. Mater.* **16**, 182–194 (2017).
40. Lin, X. et al. All-angle negative refraction of highly squeezed plasmon and phonon polaritons in graphene–boron nitride heterostructures. *Proc. Natl Acad. Sci. USA* **114**, 6717–6721 (2017).
41. Thongrattanasiri, S., Koppens, F. H. L. & Garcia de Abajo, F. J. Complete optical absorption in periodically patterned graphene. *Phys. Rev. Lett.* **108**, 047401 (2012).
42. Brar, V. W., Jang, M. S., Sherrott, M., Lopez, J. J. & Atwater, H. A. Highly confined tunable mid-infrared plasmonics in graphene nanoresonators. *Nano Lett.* **13**, 2541–2547 (2013).
43. Coldren, L. A. & Corzine, S. W. *Diode Lasers and Photonic Integrated Circuits* (Wiley, New York, NY, 2012).
44. Griffiths, D. *Introduction to Quantum Mechanics* (Pearson Prentice Hall, Upper Saddle River, NJ, 1995).
45. Glauber, R. J. & Lewenstein, M. Quantum optics of dielectric media. *Phys. Rev. A* **43**, 467–491 (1991).
46. Scheel, S. & Buhmann, S. Y. Macroscopic QED—concepts and applications. *Acta Phys. Slov.* **58**, 675–809 (2008).
47. Bitan, G. *Energy Distribution of Single and Two Photon Emitters in Plasmonic Environments*. MSc thesis, Technion IIT Department of Electrical Engineering (2014).
48. Kaminer, I. et al. Efficient plasmonic emission by the quantum Čerenkov effect from hot carriers in graphene. *Nat. Commun.* **7**, 11880 (2016).
49. Koppens, F. H. L., Chang, D. E. & Garcia de Abajo, F. J. Graphene plasmonics: a platform for strong light–matter interactions. *Nano Lett.* **11**, 3370–3377 (2011).
50. Rivera, N., Rosolen, G., Joannopoulos, J. D., Kaminer, I. & Soljačić, M. Making two-photon processes dominate one-photon processes using mid-IR phonon polaritons. *Proc. Natl Acad. Sci. USA* **114**, 13607 (2017).
51. Landau, L. D., Lifshitz, E. M. & Pitaevskii, L. P. *Electrodynamics of Continuous Media* Vol. 8 (Elsevier, New York, NY, 2008).
52. Wang, Q. H., Kalantar-Zadeh, K., Kis, A., Coleman, J. N. & Strano, M. S. Electronics and optoelectronics of two-dimensional transition metal dichalcogenides. *Nat. Nanotech.* **7**, 699–712 (2012).
53. McGill, T. C. & Collins, D. A. Prospects for the future of narrow bandgap materials. *Semicond. Sci. Technol.* **8**, S1 (1993).
54. Sloan, J., Rivera, N., Soljačić, M. & Kaminer, I. Tunable UV-emitters through graphene plasmonics. *Nano Lett.* **18**, 308–313 (2017).
55. Törmä, P. & Barnes, W. L. Strong coupling between surface plasmon polaritons and emitters: a review. *Rep. Prog. Phys.* **78**, 013901 (2014).
56. Jung, J. et al. Dyadic Green's functions of thin films: applications within plasmonic solar cells. *Phys. Rev. B* **83**, 085419 (2011).
57. Trolle, M. L. & Pedersen, T. G. Indirect optical absorption in silicon via thin-film surface plasmon. *J. Appl. Phys.* **112**, 043103 (2012).
58. Tongay, S. et al. Thermally driven crossover from indirect toward direct bandgap in 2D semiconductors: MoSe<sub>2</sub> versus MoS<sub>2</sub>. *Nano Lett.* **12**, 5576–5580 (2012).
59. Zhang, Y. et al. Direct observation of the transition from indirect to direct bandgap in atomically thin epitaxial MoSe<sub>2</sub>. *Nat. Nanotech.* **9**, 111–115 (2014).
60. Malý, P. et al. Picosecond and millisecond dynamics of photoexcited carriers in porous silicon. *Phys. Rev. B* **54**, 7929–7936 (1996).

## Acknowledgements

The authors thank M. Hoffman for the illustration in Fig. 1a and R. Tenne for his advice. The research of J.D.J. and M.S. was supported as part of the Army Research Office through the Institute for Soldier Nanotechnologies under contract no. W911NF-18-2-0048 (photon management for developing nuclear-TPV and fuel-TPV mm-scale-systems), and also supported as part of the S3TEC, an Energy Frontier Research Center funded by the US Department of Energy under grant no. DE-SC0001299 (for fundamental photon transport related to solar TPVs and solar-TEs). The research of M.O. was supported by the the Israeli ICore Excellence Center 'Circle of Light'. N.R. was supported by Department of Energy Fellowship DE-FG02-97ER25308. T.C. acknowledges support from the Danish Council for Independent Research (grant no. DFF-6108-00667). I.K. was supported by the Azrieli foundation as an Azrieli Fellow, and was partially supported by the Seventh Framework Programme of the European Research Council (FP7-Marie Curie IOF) under grant no. 328853-MC-BSiCS.

## Author contributions

All authors made significant contributions to writing the manuscript.

## Competing interests

The authors declare no competing interests.

## Additional information

**Supplementary information** is available for this paper at <https://doi.org/10.1038/s41566-018-0176-6>.

**Reprints and permissions information** is available at [www.nature.com/reprints](http://www.nature.com/reprints).

**Correspondence and requests for materials** should be addressed to Y.K. or I.K.

**Publisher's note:** Springer Nature remains neutral with regard to jurisdictional claims in published maps and institutional affiliations.

## Methods

**Considerations of plasmonic losses.** The plasmon dispersion is presented in Fig. 1b via the imaginary part of the reflectance (colourmap), computed from the full local conductivity of graphene (that is, including both intraband and interband dispersion) calculated from the random phase approximation<sup>28,49</sup>. The dashed lines give the associated intraband approximation, equation (2), neglecting losses. The excellent agreement between the two conductivity models illustrates that for the range of parameters considered in this work, the intraband (or Drude) treatment is completely sufficient. This result can be used whenever the Fermi level is larger than the plasmon energy and the influence of both intrinsic graphene non-locality and interband corrections are negligible<sup>28–30</sup>. The intrinsic graphene losses considered in Fig. 1b and in our results below reflect an intrinsic decay time of  $\tau = 0.2$  ps. This is a reasonable estimate of the decay time attainable in current experimental set-ups<sup>61</sup>, with even higher decay times attainable under cryogenic

conditions or via hexagonal boron nitride encapsulation<sup>33</sup>. For corrections due to a change in graphene losses (different Drude decay times  $\tau$ ), see Supplementary Fig. 6. In practice, these losses translate to plasmon propagation lengths on the order of a micrometre for the Fermi levels and frequencies considered here. For more details about the plasmonic losses see Supplementary Section 8.

**Data availability.** The data that support the plots within this paper and other findings of this study are available from the corresponding authors upon reasonable request.

## References

61. Tan, Y. W. et al. Measurement of scattering rate and minimum conductivity in graphene. *Phys. Rev. Lett.* **99**, 246803 (2007).